Oxygen Vacancy Ordering Phenomena in the Mixed-Conducting Hexagonal Perovskite $Ba_7Y_2Mn_3Ti_2O_{20}$

Xiaojun Kuang,[†] Mathieu Allix,[†] Richard M. Ibberson,[‡] John B. Claridge,[†] Hongjun Niu,[†] and Matthew J. Rosseinsky*,[†]

Department of Chemistry, The University of Liverpool, Liverpool L69 7ZD, United Kingdom, and ISIS Facility, CCLRC-Rutherford Appleton Laboratory, Chilton, Didcot, Oxon OX11 0QX, United Kingdom

Received November 9, 2006. Revised Manuscript Received February 11, 2007

A 21R-type mixed conducting oxygen-deficient hexagonal perovskite $Ba_7Y_2Mn_3Ti_2O_{20}$ was synthesized and its structure characterized by variable temperature neutron powder diffraction. The structure is characterized by the presence of both BaO_2 and BaO_3 layers. In the oxygen-stoichiometric material, the vacancies are ordered in c′-BaO_2 layers. Extra oxygen is accommodated by intergrowth of the vacancy-ordered c′-BaO_2 layers with cubic c-BaO_{3-x} layers ($x \cong 1$), which have disordered 2/3 oxygen occupancy. This material displays mixed electronic and oxide ionic conduction at high temperature, and the role of the two distinct and partially occupied anion sites within the BaO_2 layers in permitting the oxygen mobility is discussed.

Introduction

Pure ionic and mixed electronic and ionic conductors (MEICs) are required for applications[1−4] in solid oxide fuel cells (SOFCs) and dense membranes for oxygen separation and syn-gas production from the oxidation of natural gas. Among known fast oxide ion conductors, oxygen-deficient $ABO_{3-\delta}$ perovskites attract extensive attention as both pure oxide ionic conductors (such as $La_{1-x}Sr_xGa_{1-y}Mg_yO_{3-\delta}$)[5] and MEIC, for example, $La_{1-x}Sr_xCo_{1-y}Fe_yO_{3-\delta}$.[4,6−8] The partial aliovalent substitution of A and/or B cations in perovskite oxides with a cubic stacking of AO_3 layers is an effective route to introduce oxygen vacancies in the anion network, thus providing a three-dimensional channel for oxide ionic conduction. However, high concentrations of dopants or oxygen vacancies can induce defect aggregation, driving structural transitions to defect-ordered lower symmetry structures, which is unfavorable for oxygen mobility; for example, at $\delta = 0.5$ in $Ba_2In_2O_5$[9] the vacancy ordered brownmillerite structure[10] forms with reduced ionic conductivity. The introduction of oxygen vacancies or aliovalent acceptor doping can introduce a hexagonal motif to the stacking of the AO_3 layers in addition to the purely cubic sequence. The oxygen vacancies can be associated with either hexagonal (h) or cubic (c) AO_3 layers. For instance, when oxygen deficiency occurs through reduction[11] or the partial substitution of Ti^{4+} by the lower-charged Mn^{3+}, Fe^{3+}, Co^{3+}, Ni^{3+}, and Ga^{3+} cations,[12,13] the ferroelectric perovskite $BaTiO_3$ transforms to a 6H-type hexagonal phase, in which the oxygen vacancies are disordered in the h-BaO_3 layers,[11,12] but no ionic conduction arising from these oxygen vacancies has been reported. Substitution of Ti^{4+} by large R^{3+} cations (R = Nd and Y) in $BaTiO_3$ induces the new 12H-type hexagonal $Ba_6R_2Ti_4O_{17}$[14] with oxygen deficiency in the cubic AO_3 layers. In the structure of $Ba_6R_2Ti_4O_{17}$, the oxygen vacancies order to form a pseudocubic (c′) BaO_2 layer in a $(c'cchcc)_2$ stacking of c-BaO_3, h-BaO_3, and c′-BaO_2 layers. The existence of the c′-layer generates TiO_4 tetrahedra connected via corner-sharing to RO_6 octahedra, which in turn share corners with face-sharing Ti_2O_9 octahedral dimers. Mixed electronic and ionic conduction above 600 °C was reported for this system,[15] which is quite unusual because oxygen ionic conduction is seldom observed in hexagonal perovskites. The mechanism of ionic conduction in $Ba_6R_2Ti_4O_{17}$ is currently unclear.

In the present study, we report a 21R-type mixed conducting oxygen-deficient hexagonal perovskite $Ba_7Y_2Mn_3Ti_2O_{20}$ with c′-BaO_2 layers. Variable temperature neutron powder diffraction (NPD) shows that the c′-BaO_2 layers with ordered oxygen vacancies can transform partially into c-BaO_{3-x} ($x \cong 1$) layers with disordered oxygen vacancies on 1/3 of the anion sites. This transformation between the oxygen vacancy

[†] The University of Liverpool.
[‡] CCLRC-Rutherford Appleton Laboratory.

(1) Boivin, J. C.; Mairesse, G. *Chem. Mater.* **1998**, *10*, 2870.
(2) Gellings, P. J.; Bouwmeester, H. J. M. *Catal. Today* **2000**, *58*, 1.
(3) Pena, M. A.; Fierro, J. L. G. *Chem. Rev.* **2001**, *101*, 1981.
(4) Balachandran, U.; Dusek, J. T.; Sweeney, S. M.; Poeppel, R. B.; Mieville, R. L.; Maiya, P. S.; Kleefisch, M. S.; Pei, S.; Kobylinski, T. P.; Udovich, C. A. *Am. Ceram. Soc. Bull.* **1995**, *74* (1), 71.
(5) Ishihara, T.; Matsuda, H.; Takita, Y. *J. Am. Chem. Soc.* **1994**, *116*, 3801.
(6) Teraoka, Y.; Nobunaga, T.; Yamazoe, N. *Chem. Lett.* **1988**, 503.
(7) Tai, L.-W.; Nasrallah, M. M.; Anderson, H. U.; Sparlin, D. M.; Sehlin, S. R. *Solid State Ionics* **1995**, *76*, 259.
(8) Tai, L.-W.; Nasrallah, M. M.; Anderson, H. U.; Sparlin, D. M.; Sehlin, S. R. *Solid State Ionics* **1995**, *76*, 273.
(9) Goodenough, J. B.; Ruiz-Diaz, J. E.; Zhen, Y. S. *Solid State Ionics*, **1990**, *44*, 21.
(10) Colville, A. A.; Geller, S. *Acta Crystallogr., Sect. B* **1971**, *27*, 2311.
(11) Sinclair, D. C.; Skakle, J. M. S.; Morrison, F. D.; Smith, R. I.; Beales, T. P. *J. Mater. Chem.* **1999**, *9*, 1327.
(12) Feteira, A.; Keith, G. M.; Rampling, M. J.; Kirk, C. A.; Reaney, I. M.; Sarma, K.; M., Alford. N.; Sinclair, D. C. *Cryst. Eng.* **2002**, *5*, 439.
(13) Dickson, J. G.; Katz, L.; Ward, R. *J. Am. Chem. Soc.* **1961**, *83*, 3026.
(14) Kuang, X.; Jing, X.; Loong, C. K.; Lachowski, E. E.; Skakle, J. M. S.; West, A. R. *Chem. Mater.* **2002**, *14* (10), 4359.
(15) Jing, X.; West, A. R. *Acta Phys.−Chim. Sin.* **2002**, *18* (7), 617.

10.1021/cm0626740 CCC: $37.00
Published on Web 04/28/2007

ordered c′-BaO_2 layers and the oxygen vacancy disordered c-BaO_{3-x} layers is reversible via a redox process. A mechanism for this transformation is proposed, and the relationship between the detailed structure of the BaO_2 layer and the ionic conduction observed at high temperature for this material is discussed in light of the transformation.

Experimental Section

Polycrystalline $Ba_7Y_2Mn_3Ti_2O_{20}$ samples were synthesized by solid-state reaction from starting materials of $BaCO_3$ (99.997%, Alfa Aesar), Y_2O_3 (99.99%, Alfa Aesar), MnO_2 (99.999%, Alfa Aesar), and TiO_2 (99.99%, Aldrich), which were weighed in stoichiometric amounts and mixed in an agate mortar and pestle in an ethanol medium. The mixture was first calcined at 1173 K overnight to release CO_2 and then fired for a further 24 h at 1473 K. The product was ground and pressed into pellets, then fired at 1673 K for 64 h with a heating and cooling rate of 5 K/min and with three intermediate grindings and pressings before reaching a final product, which is apparently single phase as characterized by X-ray powder diffraction. $Ba_7Y_2Mn_3Ti_2O_{20}$ powder was pressed into pellets (with an Avure Cold Isostatic Press) and sintered at 1823 K for 24 h on platinum foil, which resulted in dense single-phase pellets with 92% of the theoretical X-ray density. Several reactions at the nominal compositions $Ba_7Y_2Mn_{3+x}Ti_{2-x}O_{20}$ ($x = 1, 2$) with increasing substitution of Ti by Mn were carried out to investigate the possibility of solid solution.

The electron diffraction (ED) study was carried out with a JEOL 2000FX electron microscope equipped with an EDAX analyzer. Energy dispersive spectroscopy (EDS) analyses were systematically carried out during the ED study. A Panalytical X'pert Pro Multi-Purpose X-ray diffractometer (Co $K\alpha_1$ radiation $\lambda = 1.789\,01$ Å) was used to carry out the X-ray diffraction (XRD) phase assemblage identification and to collect data of a quality suitable for Rietveld refinement over the 20−130° 2θ range. Time-of-flight NPD data were collected on the high-resolution diffractometer (HRPD) at the ISIS facility (Rutherford Appleton Laboratory, U.K.). Data were first recorded at ambient temperature on the as-synthesized sample (referred to as sample 1) loaded in a standard vanadium can and then at 873 K (for ∼6 h) and 1073 K (for ∼3 h) using a furnace with a vanadium heating element. A data set was recorded at ambient temperature after online cooling in the furnace and then the sample was cooled to 77 K (using a He-flow vanadium-tailed cryostat) for a final data collection. Oxygen loss was suspected to have occurred during the high-temperature measurements in this data collection sequence as the can was unsealed and subject to dynamic vacuum (10^{-4}−10^{-6} mbar) within the furnace. Accordingly, the sample was reoxidized in O_2 flow at 1073 K for 70 h, and a further data set was collected at ambient temperature after the reoxidation. For comparison, the as-synthesized sample (referred to as sample 2) was sealed in a silica tube under high vacuum (∼10^{-5} mbar) at ambient temperature to avoid irreversible oxygen loss during the high-temperature NPD experiment. Further data sets were recorded on sample 2 at different temperatures according to the sequence ambient temperature, 45 K (using a closed-cycle refrigerator (CCR)) and 873 K, and then with on-line cooling for a final ambient-temperature measurement.

Rietveld analysis was carried out with both X-ray and neutron diffraction data using the GSAS software package[16] with the EXPGUI interface.[17] The MAPVIEW module of the WINGX software package[18] was used to re-plot the difference Fourier map using GSAS files. Bond valence sums (BVSs) were calculated by Brown and Altermatt's method.[19] Hydrogen-reduction thermogravimetry was employed to determine the oxygen content. A 13 mg sample was placed in an alumina crucible and heated in a 5% H_2−95% N_2 flow with a ∼200 mL/min flow rate from ambient temperature to 1473 K with a heating rate of 10 K/min. The samples were reduced to reach a constant weight before being cooled to ambient temperature in the same atmosphere. The thermogravimetric analysis (TGA)−differential thermal analysis instrument (EXSTAR6000) was calibrated using ZrO_2 as standard material. Magnetic measurements were carried out using a Quantum Design MPMS SQUID magnetometer under a field of 500 Oe. Zero-field-cooled (ZFC) and field-cooled (FC) data were collected over the 2−300 K temperature range. Corrections have been applied for the core diamagnetic susceptibility (5.22×10^{-4} emu/mol).[20] Infrared absorption data were collected using Perkin-Elmer RXI FTIR spectrometer in 4000−400 cm^{-1} using $Ba_7Ca_2Mn_5O_{20}$ for comparison.

Alternating current impedance spectroscopy (IS) measurements in air from ambient temperature to 1073 K were performed with a Solartron 1255B frequency response analyzer and a Solartron 1296 dielectric interface over the 10^{-2}−10^6 Hz frequency range. Prior to the IS measurements, the pellets were coated with platinum paste on each face and mounted in a sample jig equipped with a furnace, which was heated to 1073 K for 30 min to burn off the organic components and form platinum electrodes. The ZView2.8[21] software was utilized to analyze the complex impedance data and carry out the equivalent circuit fitting. The data at 873 K were collected over a partial oxygen pressure (p_{O_2}) range of 1−10^{-12} atm to measure the p_{O_2} dependence and reversibility of the conductivity. The p_{O_2} was controlled with flows of O_2, Ar, and 1% CO−99% Ar and 1% CO_2−99% Ar. The p_{O_2} in the 1−10^{-4} atm range was controlled by dilution of O_2 flow with Ar with an equilibration time range of 10−24 h, and the low p_{O_2} range of less than 10^{-4} atm was controlled by using 1% CO−99% Ar and 1% CO_2−99% Ar flows with an equilibration time of more than 12 h. Continuous measurement was carried out to ensure equilibration of the sample with the gas environment. An yttrium-stabilized ZrO_2 potentiometric sensor was used to monitor the p_{O_2} values. Oxygen ion transport numbers were measured at 773−1073 K by using air−O_2 gas concentration cells, for which specially designed double alumina tubes were employed (Figure S1, Supporting Information). Pellets with platinum electrodes and wires on each face were sealed on the outer tubes with cement (Ceramabond 503, Aremco Products, Inc., U.S.A.), and then the double alumina tubes were placed into a sealed alumina tube furnace. Figure S1 (Supporting Information) shows a schematic of the concentration cell. Initially, oxygen gas is passed through the double alumina tubes and air through the alumina tube, and then the gas flow is reversed to ensure the voltage changes sign, that is, that the sample is acting as electrolyte for oxygen ionic transport. The oxygen ion transport number was calculated from the ratio of the measured EMF from the Keithley 617 electrometer to the theoretical one from the Nernst equation for the ratio of p_{O_2} values.

(16) Larson, A. C.; Von Dreele, R. B. *General Structure Analysis System (GSAS)*; Los Alamos National Laboratory Report LAUR 86-748; Los Alamos National Laboratory: Los Alamos, NM, 2004.

(17) Toby, B. H. *J. Appl. Crystallogr.* **2001**, *34*, 210.

(18) Farrugia, L. J. *J. Appl. Crystallogr.* **1999**, *32*, 837.

(19) Brown, I. D.; Altermatt, D. *Acta Crystallogr., Sect. B* **1985**, *41*, 244.

(20) Boudreaux, E. A.; Mulay, L. N. *Theory and Application of Molecular Paramagnetism*; Wiley: New York, 1976.

(21) Scribner Associates, Inc. *Zview for Windows, Impedance/Gain Phase Graphing and Analysis Software*; Southern Pines, NC, 2001.

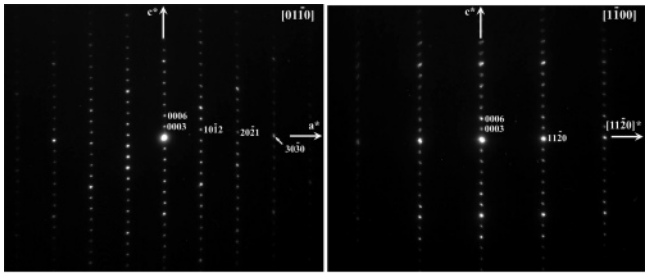

Figure 1. ED patterns of $Ba_7Y_2Mn_3Ti_2O_{20}$ along the [01$\bar{1}$0] and [1$\bar{1}$00] directions.

Results

XRD and ED. The XRD pattern reveals a hexagonal cell for as-synthesized $Ba_7Y_2Mn_3Ti_2O_{20}$: $a = 5.84$ Å, $c = 50.84$ Å. The ED result (in Figure 1) confirmed the hexagonal cell and the observed reflection conditions ($h0\bar{h}0$, $h = 3n$; $000l$, $l = 3n$; $h\bar{h}0l$, $\bar{h} + l = 3n$; and $hh\overline{2h}l$, $l = 3n$) indicate five possible space groups: $R3$ (No. 146); $R\bar{3}$ (No. 148); $R32$ (No. 155); $R3m$ (No. 160); and $R\bar{3}m$ (No. 166). EDS analyses have been carried out on 12 crystallites and give an average cation ratio of $Ba_{6.82}Y_{2.02}Mn_{2.93}Ti_{2.23}$, which is close to the ideal one. XRD patterns of $Ba_7Y_2Mn_{3+x}Ti_{2-x}O_{20}$ ($x = 1$, 2) indicated a mixture of $Ba_7Y_2Mn_3Ti_2O_{20}$ and a 12R-phase ($Ba_4YMn_3O_{11.5}$)[22] at $x = 1$ and the 12R-phase (with disappearance of the 21R phase) at the nominal composition $Ba_7Y_2Mn_5O_{20}$ ($x = 2$).

Hydrogen-reduction TGA on the as-synthesized sample (Figure S2, Supporting Information) gave a 2.8(1)% mass loss, which is consistent with the mass loss of 2.79% expected for the nominal composition by assuming the Mn has been completely reduced to Mn^{2+} and Ti remains as Ti^{4+} in the final product, thus confirming the oxygen content as 20 per formula within error for the as-synthesized sample. XRD and ED of the final product after TGA reduction revealed a polyphasic material, in which the main phase is a cubic perovskite (with an approximate cation ratio of BaYMnTi).

The *c*-axis length suggests a 21-layer structure for $Ba_7Y_2Mn_3Ti_2O_{20}$, similar to that observed for $Ba_7Ca_2Mn_5O_{20}$,[23] which consists of c-BaO_3, h-BaO_3, and c′-BaO_2 layers with a stacking sequence of $(ccc'cch_2)_3$ along the *c*-axis. Rietveld analysis of XRD data was carried out using the structural model (Figure 2) of $Ba_7Ca_2Mn_5O_{20}$ in the highest symmetry $R\bar{3}m$ space group permitted by the systematic absences. In this model there are four distinct sets of sites occupied by the Y, Mn, and Ti cations: the M2 sites are tetrahedral in the starting model (coordination by three oxide from a c layer and one oxide from a c′ layer), while the M3 and M1 are terminal and central octahedral sites in the face-sharing trimer and Y occupies a corner-sharing site linking the trimer to the M2 site. The development of a correct description of the coordination at the M2 site will turn out to be the key part of the structure determination. The refinement confirms this structure (Figure S3, Supporting Information) but results

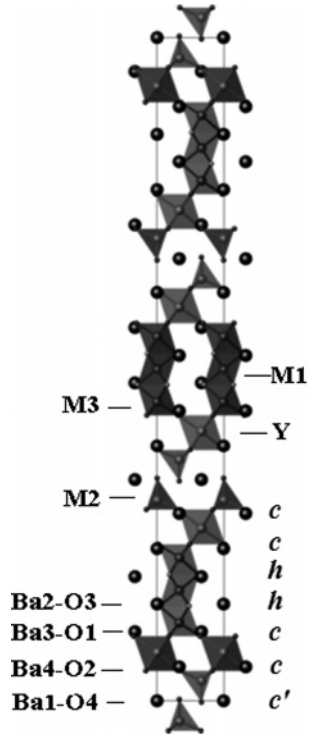

Figure 2. Projection of the initial structural model for $Ba_7Y_2Mn_3Ti_2O_{20}$ along (1$\bar{2}$10).

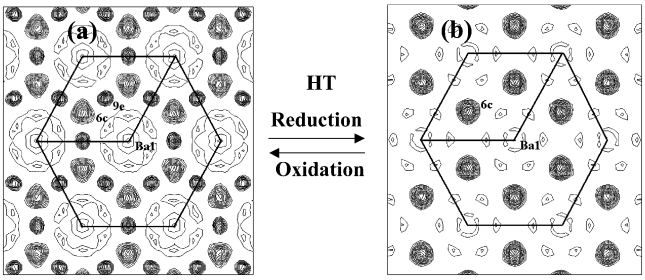

Figure 3. $z = 0$ sections of the difference Fourier map calculated with all atoms except for O4 in the model for as-synthesized (a) and reduced (b) $Ba_7Y_2Mn_3Ti_2O_{20}$ sample 1 at ambient temperature.

in a very high U_{iso} (~0.60 Å^2) for the oxygen O4 on the 6c sites along the 3-fold axis in the c′-BaO_2 layers. This suggests possible partial occupancy of the 6c site or that this site is not the correct position for O4. Refinement of powder neutron diffraction data is used to resolve this question.

Ambient Temperature Structure of the As-Synthesized Sample. The refined atomic displacement parameter for O4 at the 6c sites from the ambient temperature NPD data for as-synthesized $Ba_7Y_2Mn_3Ti_2O_{20}$ (sample 1) is anomalously high ($U_{iso} \sim 0.16$ Å^2), and lowering the symmetry to $R3m$, $R\bar{3}$, and $R3$, or to the monoclinic space groups $C2/m$ and Cm did not solve this problem. A difference Fourier map was calculated with all atoms except for O4, and the $z = 0$ section is shown in Figure 3a. Two obvious residual peaks were observed around the initially used 6c site and at the 9e sites which is not present in the initial model. With the new position O5 at the 9e sites, the refinement was improved ($\chi^2 \sim 1.57$ and 1.87 with and without O5, respectively) and the U_{iso} values for O4 and O5 were reduced to ~0.0142 Å^2 (U_{iso} values for O4 and O5 are constrained to be equal in the refinement). However, the refined occupancy values at the 6c and 9e sites, 0.474(8) and 0.256(5), respectively, lead to

(22) Kuang, X.; Bridge, C.; Allix, M.; Claridge, J. B.; Hughes, H.; Rosseinsky, M. J. *Chem. Mater.* **2006**, *18*, 5130.
(23) Floros, N.; Michel, C.; Hervieu, M.; Raveau, B. *J. Solid State Chem.* **2002**, *168*, 11.

a BaO_{2-x} layer composition, which is not reasonable from a chemical coordination viewpoint as this would result in an average coordination number of less than 4 for the M2 sites and a total oxygen content (19.72(3)) of less than 20 per formula unit. A general site (36i) around the ideal 6c site was employed for the O4 atoms at the next stage of the refinement, which slightly improved the fitting (χ^2 was reduced to 1.49) and resulted in occupancies at 36i and 9e sites of 0.112(3) and 0.253(8) and a total oxygen content of 20.07(8) per formula, which agrees well with the TGA result within experimental error.

The distances between the O4 6c and O5 9e sites are too short (~1.7 Å) for simultaneous occupancy of both sites to occur in a single layer. The occupancy of both 6c (36i) and 9e sites suggests there is a mixture of two distinct layer types: c′-BaO_2 layers associated with O4 at the 6c (36i) sites and c-BaO_{3-x} layers associated with O5 at the 9e sites. According to the overall oxygen content, the c-BaO_{3-x} layer must have an oxygen content of 2 with 2/3 occupancy of the O5 sites within the layer. This disordered layer is subsequently referred to as a c_p-BaO_2 layer (p denoting partial occupancy). The existence of mixed c′-BaO_2 and c_p-BaO_2 layers results in partial oxygen vacancy disordering in the Ba1−O4(O5) layers and two kinds of coordination environments for the M2 sites in the as-synthesized sample 1: these are tetrahedral, centered around c′-BaO_2 layers where M2 is coordinated by one O4 atom from the c′-BaO_2 layer and three O2 atoms, and pyramidal, centered around the c_p-BaO_2 layers where M2 is coordinated by two O5 atoms and three O2 atoms. The tetrahedra are isolated while the pyramids are corner-sharing within the layer.

Using one site to represent the location of the M2 cation gave a relatively short bond length (1.652(8) Å) in the $M2O_4$ tetrahedron and a relatively long bond length (2.252(3) Å) in the pyramidal $M2O_5$ unit. The refined anisotropic displacement parameters (Å^2) for the M2 site ($U_{11} = U_{22} = 0.002(1)$, $U_{33} = 0.020(3)$, $U_{12} = 0.0009(7)$, $U_{13} = U_{23} = 0$) show an apparent displacement along the *c*-axis compared with the other directions for the M2 atoms. Therefore, the M2 sites were split into two sites to reflect the two different coordination environments, a tetrahedral M2′ and a pyramidal M2″ site with occupancies fixed according to the oxygen occupancies at the O4 (36i) and O5 (9e) sites, respectively. The refined fractional coordinates for M2′ and M2″ show an 0.22(3)Å separation along the 3-fold axis. This splitting of the M2 site gives more reasonable bond lengths; that is, the short bond length in $M2'O_4$ increases to 1.71(2)Å and the long bond length in $M2''O_5$ decreases to 2.15(2)Å. However, the BVSs for the pyramidal M2″ (~3.10 for Ti^{4+} and ~2.62 for Mn^{4+}) are not chemically sensible. Moving the pyramidal M2″ site off the 3-fold axis only slightly improved the bond lengths. Finally, optimal structural parameters were achieved by moving O5 off the special site 9e into a general site 36i in $R\bar{3}m$ as well as splitting Ba1 into two sites Ba1′ (3a) and Ba1″ (36i) corresponding to occupation of the O4 and O5 sites, respectively. This suggested that the O5 site disorder around the 9e sites (the distance between the 36i and 9e sites is ~0.26 Å) gives one short bond length (1.92(2) Å) and one long bond (= 2.41-(2) Å) for M2″−O5. Attempts to use the acentric space groups *R*3*m* or *Cm* did not improve the bond lengths associated with the pyramidal M2″ site. Refinement reveals that the Ba1″ species occupies the special 6c position. The O5 splitting site is consistent with the disordered distribution of c′-BaO_2 layers (Ba1′−O4) and c_p-BaO_2 layers (Ba1″−O5) as the interlayer distance from the neighboring BaO_3 layers to the c_p-BaO_2 layers is, at ~2.1−2.2 Å, much shorter than that between BaO_3 and the neighboring c′-BaO_2 layer of ~2.6 Å. This makes the local distances from the Ba1′−O4 and Ba1″−O5 layers to the neighboring BaO_3 layers different; that is, there are locally compressed and expanded interlayer distances between respectively c_p-BaO_2 layers and c′-BaO_2 layers from the neighboring BaO_3 layers. However, using the present diffraction data only an average structure and not the local structural details can be refined. Locally O5 must be midway between two pyramidal M2″ sites in neighboring layers, and the bond lengths for M2″−O5 are 1.92(2) Å. This leads to a reasonable BVS of 3.92 for pyramidal Ti^{4+}, although the BVS for Mn^{4+} (3.31) is not reasonable for occupancy of this site, nor is the long bond length of 2.41(2) Å meaningful. The final structural parameters and selected bond lengths for the as-synthesized sample 1 at ambient temperature are listed in Tables 1 and 2, respectively. The Rietveld refinement of the NPD data at ambient temperature for the as-synthesized sample 1 is shown in Figure 4. The structure for the as-synthesized sample 2 at ambient temperature is similar to that for sample 1, as the mixed c′-BaO_2 and c_p-BaO_2 layers were observed also in the as-synthesized sample 2 at ambient temperature.

Table 1. Final Structural Parameters for As-Synthesized $Ba_7Y_2Mn_3Ti_2O_{20}$ Sample 1 at Ambient Temperature[a]

atom	site	*x*	*y*	*z*	U_{iso} (Å^2)	occupancy
Ba1′	3a	0	0	0	0.0041(5)	0.616(2)[b]
Ba1″	6c	0	0	0.0036(4)	0.0041(5)	0.192(1)[b]
Ba2	6c	0	0	0.14603(7)	0.0041(5)	1
Ba3	6c	0	0	0.22939(7)	0.0041(5)	1
Ba4	6c	0	0	0.38443(6)	0.0041(5)	1
Y	6c	0	0	0.07326(6)	0.0081(5)	1
M1	3b	0	0	0.5	0.0016(7)	1 unit[c]
M2′	6c	0	0	0.6976(2)	0.0016(7)	0.616(5)[b] unit[c]
M2″	6c	0	0	0.6934(4)	0.0016(7)	0.384(5)[b] unit[c]
M3	6c	0	0	0.45071 (9)	0.0016(7)	1 unit[c]
O1	18h	0.1775(2)	0.8225(2)	0.09728(3)	0.0065(5)	1
O2	18h	0.4962(3)	0.5038(3)	0.37842(3)	0.0126(4)	1
O3	18h	0.1473(2)	0.8527(2)	0.47644(3)	0.0048(4)	1
O4	36i	0.068(2)	0.006(3)	0.3356(1)	0.003(3)	0.102(1)[d]
O5	36i	0.52(1)	0.048(3)	0.0018(4)	0.003(3)	0.064(1)[d]

[a] Space group: $R\bar{3}m$, $a = 5.84265(2)$ Å, $c = 50.8562(4)$ Å, $Z = 3$. $R_{wp} = 5.67\%$, $R_p = 5.06\%$, $R_F^2 = 5.20\%$, $\chi^2 = 1.49$ for 37 variables. The U_{iso} values are constrained to be identical for the same type of elements except for oxygen. [b] The occupancies for the Ba1′ and Ba1″ and M2′ and M2″ sites were constrained according to the occupancies of the O4 and O5 sites, respectively. [c] In each case, a statistical mixture of 0.6 Mn and 0.4 Ti was used at each M site (referred to as 1 unit) and reduced in occupancy according to the refined values for the O4 and O5 sites. [d] The occupancies of the O4 and O5 sites are constrained according to the total oxygen content as two per Ba1′(Ba1″)−O4(O5) layer.

Ambient Temperature Structure for Reduced Sample 1. After heating to 873 K for 6 h under dynamic vacuum during the NPD experiment then cooling to ambient temperature, the NPD data from sample 1 show that the unit cell of $Ba_7Y_2Mn_3Ti_2O_{20}$ has expanded to 1519.05(2) Å^3 from 1503.47(2) Å^3 before heating and cooling. This can be

Table 2. B−O (B = Y, Ti, Mn), and Mn(Ti)−Mn(Ti) Distances (Å) and Selected Bond Angles (°) for As-Synthesized $Ba_7Y_2Mn_3Ti_2O_{20}$ Sample 1 at Ambient Temperature

bond	length	bond	length/angle
Y−O1 (×3)	2.173(3)	M2′−M2″	0.22(3)
Y−O2 (×3)	2.242(3)	M1−M3	2.507(5)
M1−O3 (×6)	1.913(2)	O2−M2″−O2 (×3)	97.7(7)
M2′−O2 (×3)	1.799(5)	O2−M2″−O5 (×2)	88.8(1)
M2′−O4 (×1)	1.73(1)	O2−M2″−O5 (×2)	91.0(2)
M2″−O2 (×3)	1.90(1)	O5−M2″−O5 (×1)	81.3(1)
M2″−O5 (×2)	1.92(2)	O2−M2′−O2 (×3)	105.1(5)
M3−O1 (×3)	1.879(3)	O2−M2′−O4 (×1)	123.8(6)
M3−O3 (×3)	1.984(3)	O2−M2′−O4 (×1)	102.0(4)
		O2−M2′−O4 (×1)	114.0(6)

ascribed to a small amount of oxygen loss under low oxygen partial pressure. Refinement of the ambient temperature data of this reduced $Ba_7Y_2Mn_3Ti_2O_{20}$ sample was carried out with the initial model of Figure 2 and results in a similarly large atomic displacement parameter $U_{iso} \sim 0.10$ Å^2 for O4 at the 6c site. Use of anisotropic atomic displacement parameters for O4 did not improve the refinement. The difference Fourier map (in Figure 3b) calculated with all atoms except for O4 shows only residual peaks around the 6c sites and no obvious residual peaks at the 9e sites, which suggests that the Ba1−O4 layers are pure c′-BaO_2 layers in this case and that the oxygen vacancies are ordered. The peak around the 6c sites confirms that the M2 atoms are in tetrahedral coordination, but refinement suggests partial occupation of the 6c sites, which is not reasonable as it would result in a coordination number of less than 4 for the M2 site. Therefore a general site (36i) around the ideal 6c site was employed for the O4 atoms, with an occupancy of 1/6 to ensure tetrahedral coordination for the M2 site. This produces a reasonable $U_{iso} \sim 0.018$ Å^2 for the O4 atoms. Refinement of the occupancies at the other three oxygen sites O1, O2, and O3 did not reveal significant vacancy concentration. The final structural parameters and selected bond lengths for this reduced sample 1 at ambient temperature are listed in Tables 3 and 4, respectively. The refined oxygen contents of the as-synthesized material and the material treated under dynamic vacuum must differ by less than the precision of the present neutron data, as the as-synthesized material has a refined oxygen content (20.07(8)) that lies within error of the dynamic vacuum treated material. No obvious change in color was observed as a result of the oxygen loss. When the reduced sample was reoxidized under flowing oxygen at 1073 K for 70 h, in the subsequent ambient temperature refinement, the cell volume was smaller than that of the reduced material at ambient temperature and the oxygen atoms in the Ba1−O4 layers were found occupying both the 6c and the 9e sites, which suggests that after reoxidation the Ba1−O4 layers revert to the mixed c′-BaO_2 and c_p-BaO_2 layers as found in the as-synthesized sample 1. Oxidation in flowing O_2 at 1073 K for 48 h and hydrogen-reduction TGA were carried out to detect the mass variation for the reduced and reoxidized samples, respectively. No significant mass gain was found from the oxygen-oxidation TGA data for the reduced sample, and the oxygen content from hydrogen-reduction TGA on the reoxidized sample did not show significant difference from that of the as-synthesized sample. This suggests the oxygen content variations due to the redox processing are too small to detect, consistent with the neutron result.

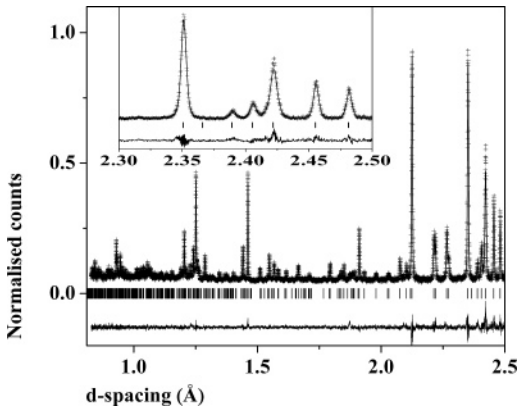

Figure 4. Rietveld refinement of the ambient temperature NPD data from the back-scattering detector for as-synthesized $Ba_7Y_2Mn_3Ti_2O_{20}$ sample 1. Inset is the enlarged plot in the 2.3−2.50 Å range. Tick marks indicate the positions of the Bragg reflections.

High-Temperature Structure and Temperature Dependence of Oxygen Vacancy Distribution of Samples 1 and 2. Variable temperature NPD data recorded in the range 45−1073 K give no evidence for a phase transition in $Ba_7Y_2Mn_3Ti_2O_{20}$. The data at 873 K, collected on the unsealed sample 1 and the sealed sample 2, show similar high atomic displacement U_{iso} values (>0.09 Å^2) for O4 at the 6c sites, and difference Fourier maps were the same as those observed for the reduced sample 1 at ambient temperature. Apparently the Ba1−O4 layers at high temperature for both the sealed and the unsealed samples are pure c′-BaO_2 layers instead of mixed c′-BaO_2 and c_p-BaO_2 layers, and the oxygen vacancies at high temperature are ordered. A similar model to the ambient temperature refinement of the reduced sample 1 was employed for the high-temperature structure refinement. There is no significant difference between the structural parameters from sample 1 and those from sample 2 at high temperature. The final structural parameters and selected bond lengths for the unsealed sample 1 at 873 K are listed in Tables S3 and S4, Supporting Information, respectively.

For the reduced sample 1, the 77 K data reveal pure c′-BaO_2 layers with ordered oxygen vacancies similar to the structure found at ambient temperature. For the as-synthesized sample 2, a similar mixture of vacancy-ordered c′-BaO_2 and vacancy-disordered c_p-BaO_2 layers as found at ambient temperature was observed at 45 K. The ambient temperature data collected on sample 2 after the 1073 K measurement shows disordered layers and slight cell parameter expansion (∼0.1% of the unit cell volume) when compared with initial ambient temperature data set, which indicated that sealing in the silica tube effectively prevents irreversible oxygen loss from sample 2. The temperature dependences of the unit cell volumes of $Ba_7Y_2Mn_3Ti_2O_{20}$ and the status of oxygen vacancy ordering at each temperature for each sample are shown in Figure 5.

Conductivity Characterization. The impedance data at ambient temperature indicated that the $Ba_7Y_2Mn_3Ti_2O_{20}$ pellet has a high relative permittivity (from 40 to 47 in the 10^3−10^6 Hz range), which is comparable with that for $BaMn_{1/2}$-

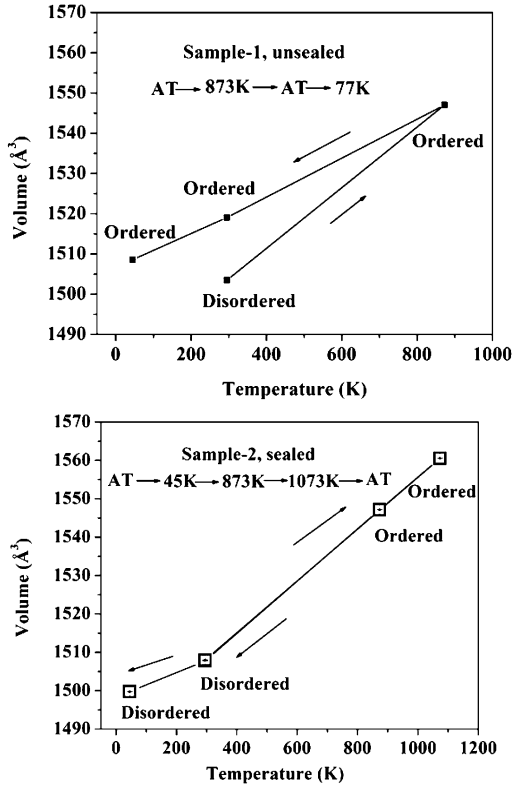

Figure 5. Temperature dependences of the unit cell volumes of $Ba_7Y_2Mn_3Ti_2O_{20}$ samples 1 and 2. The temperature sequence for variable temperature NPD experiments and the oxygen vacancy status within the Ba1′(Ba1″)−O4(O5) layers (ordered or disordered) for each sample at each temperature are labeled. AT denotes ambient temperature. The legend indicates the sequence of measurement.

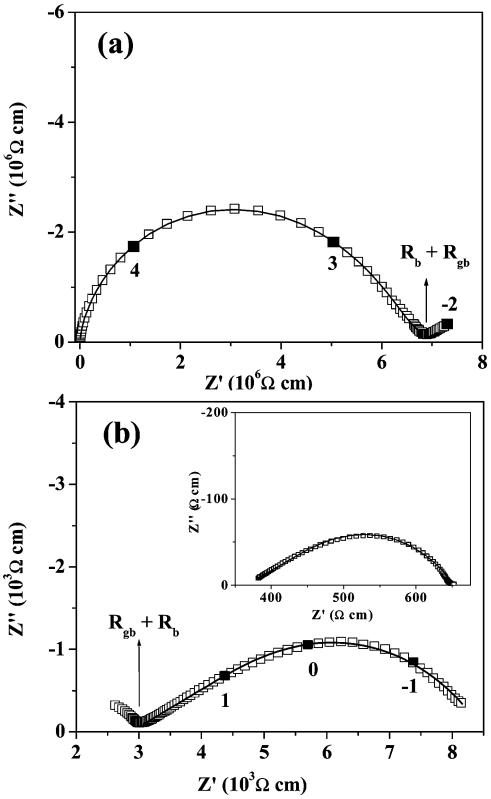

Figure 6. Complex impedance $Z''-Z'$ plots of $Ba_7Y_2Mn_3Ti_2O_{20}$ at 473 K (a) and 773 K (b). The selected frequency logarithms are shown as numbers. The $Z''-Z'$ plot at 973 K is shown in the inset of part b. The calculated and experimental data are represented by the solid lines and symbols, respectively.

$Ti_{1/2}O_3$.[24] Below 473 K, the impedance data comprise bulk and grain boundary responses, which overlap in the complex impedance Z″−Z′ plot and are modeled with an equivalent circuit consisting of a serial combination of two circuits with three parallel R_i, C_i, and $(CPE)_i$ elements (i is b for bulk or gb for grain boundary, and CPE is a constant phase element).[21] The extraction of the bulk and grain boundary components is illustrated in Figure S5, Supporting Information, for the impedance data at 398 K. Figure 6a shows the complex impedance data of $Ba_7Y_2Mn_3Ti_2O_{20}$ at 473 K. The fitting gave $R_b \sim 6.7 \times 10^6$ Ω cm, $C_b \sim 4.5$ pF/cm, $R_{gb} \sim 3.7 \times 10^5$ Ω cm, and $C_{gb} \sim 24$ pF/cm, which suggests that the grain boundary is more conductive than the grains. Therefore, the intercept on the Z' axis can be treated as the bulk resistivity as R_{gb} is much less than R_b and $R_{gb} + R_b \approx R_b$. The electrode response emerges (a ∼30° linear tail in the low-frequency range (10^{-2}−10 Hz)) once the temperature is above 473 K. With increasing temperature, the arc from bulk and grain boundary responses vanished gradually, and electrode response dominated the impedance data. Above 773 K, the high frequency intercept on the Z' axis was treated as the bulk resistivity. The Arrhenius plot for the bulk conductivity (in Figure 7a) leads to an activation energy of 0.80 eV. At high temperature above 620 K, the capacitance in the low-frequency range of $10^{-2}-1$ Hz varied within $\sim 10^{-1}-10^2$ μF/cm, which is a typical electrical double-layer phenomenon.[25] This large capacitance suggested that the diffusion process and charge-transfer reaction could occur at the sample−electrode interface, that is; the material could exhibit mixed electronic and ionic conduction. In 873−1073 K, the oxygen ion transport number was measured with an air/O_2 concentration cell varied within 0.37−0.40 (Figure 7b), which confirmed the mixed electronic and ionic conduction for $Ba_7Y_2Mn_3Ti_2O_{20}$. At 773 K, a clear half tear-drop-shaped arc was observed (Figure 6b), which is a characteristic feature of the impedance response of mixed electronic and ionic conduction.[26] A generalized finite Warburg (GFW) element[21,26] $Z_W = R_w \tanh((iT_w\omega)^n)/(iT_w\omega)^n$ was used to model this electrode response, where the R_w and T_w parameters are associated with the oxygen ionic charge transfer and diffusion and $0 < n < 1$. The fitting of the 773 K impedance data in Figure 6b resulted in $R_w \sim 5.6 \times 10^3$ Ω cm, $T_w \sim 1.53$ s, and $n \sim 0.27$ for the GFW element. The parameter n in GFW is approximately half of that for the infinite length Warburg element, 0.5.[21] The measurement of the impedance as function of p_{O_2} reveals a significant divergence when measured on decreasing and increasing p_{O_2} once the p_{O_2} became lower than 10^{-4} atm. This could be due to slight decomposition under the low p_{O_2} or CO_2-containing environment, although XRD only shows the 21R-phase after treatment by 1% CO in Ar for more than 48 h. Reduction by 5% H_2 in N_2 at 1273 K for more than 50 h

(24) Keith, G. M.; Kirk, C. A.; Sarma, K.; Alford, N. M.; Cussen, E. J.; Rosseinsky, M. J.; Sinclair, D. C. *Chem. Mater.* **2004**, *16*, 2007.

(25) Irvine, J. T. S.; Sinclair, D. C.; West, A. R. *Adv. Mater.* **1990**, *2* (3), 132.

(26) Lai, W.; Haile, S. M. *J. Am. Ceram. Soc.* **2005**, *88* (11), 2979.

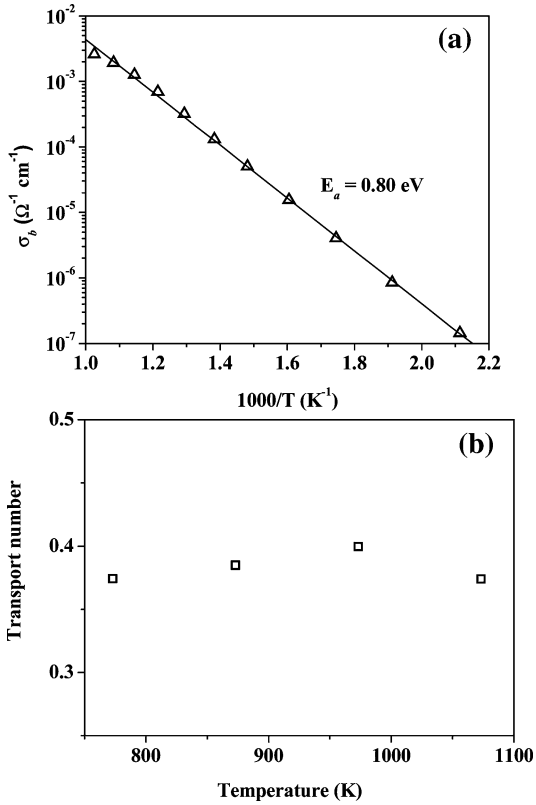

Figure 7. (a) Temperature dependence of the bulk conductivity measured in air and (b) the oxygen transport number as a function of temperature for a 92% dense $Ba_7Y_2Mn_3Ti_2O_{20}$ pellet.

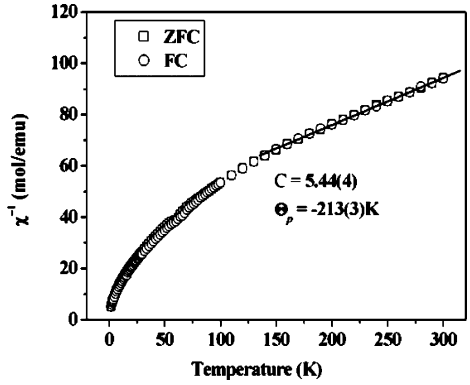

Figure 8. Temperature dependence of the inverse susceptibility of $Ba_7Y_2Mn_3Ti_2O_{20}$. The solid line is a fit to the Curie−Weiss law.

leads to a polyphasic material in which the main phase is a cubic perovskite. Over the p_{O_2} range $1-10^{-4}$ atm, the conduction exhibits p-type behavior, for which the bulk conductivity as a function of p_{O_2} is shown in Figure S6, Supporting Information.

Magnetic Behavior and Infrared Absorption Spectra. The temperature dependence of the inverse magnetic susceptibility of $Ba_7Y_2Mn_3Ti_2O_{20}$ (Figure 8) shows paramagnetic behavior over the 150−300 K range. The Curie−Weiss fit gives an effective moment of 3.81(2) μ_B per Mn, consistent with the Mn^{4+} oxidation state though slightly lower than the expected value of 3.89 μ_B, and a Weiss constant, Θ_p, of −213(3) K, which reveals strong antiferromagnetic interactions between the Mn^{4+} cations in the trimers. This negative Θ_p is consistent with those observed in $Ba_7Ca_2Mn_5O_{20}$[23] and some materials with the face-sharing trimer Mn_3O_{12} unit, for example, $BaTi_{1/2}Mn_{1/2}O_3$[24] and $Ba_4YMn_3O_{11.5}$.[22] There is a small ZFC/FC divergence below ~80 K, which is difficult to interpret due to the presence of a minor impurity hexagonal $YMnO_3$ phase,[27] which was detected by the transmission electron microscopy and EDS analyses, although there are no apparent reflections in XRD and NPD data. The infrared absorption spectra of $Ba_7Y_2Mn_3Ti_2O_{20}$ and $Ba_7Ca_2Mn_5O_{20}$ (Figure S7, Supporting Information) exhibit similar absorption bands in the 400−1000 cm^{-1} range, which agree well with the reported ones for $Ba_6Y_2Ti_4O_{17}$[14] with TiO_4 units and $Ba_4Ca_{1-x}Mn_{3+x}O_{12-\delta}$[28] with MnO_4 units. The absorption band at 863 cm^{-1} for $Ba_7Y_2Mn_3Ti_2O_{20}$ and 854 cm^{-1} for $Ba_7Ca_2Mn_5O_{20}$ (850 cm^{-1} from TiO_4 in $Ba_6Y_2Ti_4O_{17}$, 856 cm^{-1} from MnO_4 in $Ba_4Ca_{1-x}Mn_{3+x}O_{12-\delta}$) can be assigned to the tetrahedral stretching mode. In the higher wavenumber range 1000−4000 cm^{-1}, no significant hydroxyl and carbonate group absorptions were detected.

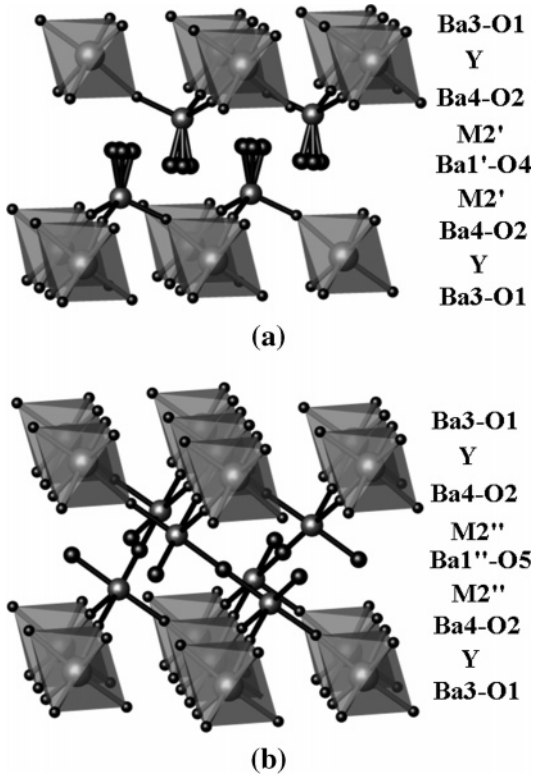

Figure 9. Local structure around the M2 site. The tetrahedron $M2'O_4$ formed by the c′-BaO_2 layer (a) with O4 disordered over six positions near the 6c site. The pyramid $M2''O_5$ formed by the c_p-BaO_2 layer (b). The Ba atoms are omitted for clarity.

Discussion

Transformation between c′-BaO_2 and c_p-BaO_2 Layers. In the ambient temperature structure of as-synthesized $Ba_7Y_2Mn_3Ti_2O_{20}$ sample 1, the occupancies at the O4 and O5 sites suggest that there are ~62% vacancy-ordered c′-BaO_2 layers and ~38% vacancy-disordered c_p-BaO_2 layers. This disordered distribution of the c′-BaO_2 layers and the c_p-BaO_2 layers means the M2 sites can move to accommodate either

(27) Tomuta, D. G.; Ramakrishnan, S.; Nieuwenhuys, G. J.; Mydosh, J. A. *J. Phys.: Condens. Matter* **2001**, *13*, 4543.
(28) Floros, N.; Michel, C.; Hervieu, M.; Raveau, B. *Chem. Mater.* **2000**, *12*, 3197.

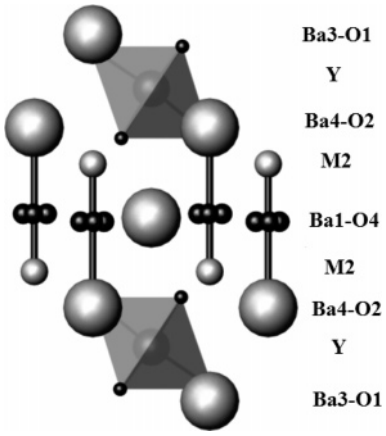

Figure 10. Schematic plot showing the O4 site splitting and the Ba4−M2 arrays on the 3-fold axis in $Ba_7Y_2Mn_3Ti_2O_{20}$.

Table 3. Final Structural Parameters for the Reduced $Ba_7Y_2Mn_3Ti_2O_{20}$ Sample 1 at Ambient Temperature[a]

atom	site	*x*	*y*	*z*	U_{iso} (Å^2)	occupancy
Ba1	3a	0	0	0	0.0074(6)	1
Ba2	6c	0	0	0.1464(1)	0.0074(6)	1
Ba3	6c	0	0	0.2288(1)	0.0074(6)	1
Ba4	6c	0	0	0.38480(8)	0.0074(6)	1
Y	6c	0	0	0.07390(7)	0.0068(6)	1
M1	3b	0	0	0.5	0.0029(7)	1 unit
M2	6c	0	0	0.6970(1)	0.0029(7)	1 unit
M3	6c	0	0	0.4505(1)	0.0029(7)	1 unit
O1	18h	0.1771(3)	0.8229(3)	0.09741(4)	0.0090(6)	1
O2	18h	0.4972(4)	0.5028(4)	0.37851(4)	0.0210(6)	1
O3	18h	0.1481(2)	0.8519(2)	0.47660(4)	0.0058(5)	1
O4	36i	0.005(2)	0.076(2)	0.3351(1)	0.018(3)	1/6

[a] Space group: $R\bar{3}m$, $a = 5.85820(2)$ Å, $c = 51.1109(4)$ Å, $Z = 3$. $R_{wp} = 4.40\%$, $R_p = 3.90\%$, $R_F^2 = 6.64\%$, $\chi^2 = 1.38$ for 37 variables. A statistical mixture of 0.6 Mn and 0.4 Ti was used at each M site, described as 1 unit as in Table 1.

tetrahedral or pyramidal coordination, giving oxygen access to two different sites O4 and O5 within the layer. The local structures around the c′-BaO_2 layers with M2 tetrahedra and the c_p-BaO_2 layers with M2 pyramids are illustrated in Figure 9a,b, respectively.

The slight reduction under dynamic vacuum at 873 K causes the mixed *c*′-BaO_2 and c_p-BaO_2 layers in the as-synthesized sample 1 to convert into pure c′-BaO_2 layers which are retained at ambient temperature after cooling; that is, in the reduced sample 1 the oxygen vacancies in the Ba1−O4 layers become ordered and the M2 site shows only the tetrahedral coordination environment, without the pyramidal one. The sealing of the as-synthesized sample in the silica tube prevented irreversible oxygen loss at high temperature in the NPD experiment, and the mixed c′-BaO_2 and c_p-BaO_2 layers still survived after cooling to ambient temperature due to reabsorption of the oxygen on cooling. Once the reduced sample was reoxidized at 1073 K, the pure c′-BaO_2 layers become mixed c′-BaO_2 and c_p-BaO_2 layers at ambient temperature. All these structural variations for $Ba_7Y_2Mn_3Ti_2O_{20}$ suggest that the c′-BaO_2 and c_p-BaO_2 layers can interconvert by small redox-based changes. The partial oxygen pressure has a strong effect on the oxygen vacancy order within the oxygen-deficient layers. The transformation between the oxygen vacancy ordered c′-BaO_2 and the oxygen vacancy disordered c_p-BaO_2 layers in $Ba_7Y_2Mn_3Ti_2O_{20}$ through this redox processing is quite unusual for the oxygen deficient hexagonal perovskite. A mechanism based on oxygen nonstoichiometry can be proposed as follows for this transformation between the c′-BaO_2 and c_p-BaO_2 layers, as described by the following reaction.

Table 4. B−O (B = Y, Ti, Mn), Ba−Mn(Ti), and Mn(Ti)−Mn(Ti) Bond Lengths (Å) and Selected Bond Angles (°) for the Reduced $Ba_7Y_2Mn_3Ti_2O_{20}$ Sample 1 at Ambient Temperature

bond	length	bond	length/angle
Y−O1 (×3)	2.162(3)	Ba4−M2′	4.19(1)
Y−O2 (×3)	2.261(4)	M1−M3	2.530(6)
M1−O3 (×6)	1.921(2)	O2−M2−O2 (×3)	104.0(2)
M2−O2 (×3)	1.827(4)	O2−M2−O4 (×1)	127.4(3)
M2−O4 (×1)	1.697(8)	O2−M2−O4 (×1)	104.0(2)
M3−O1 (×3)	1.879(5)	O2−M2−O4 (×1)	112.8(4)
M3−O3 (×3)	2.010(5)		

$$c'\text{-}BaO_2 + 0.5xO_2(g) = c_p\text{-}BaO_{2+x} \quad (1)$$

In the as-synthesized sample and the reoxidized sample, the c_p-BaO_{2+x} layers contain a small amount of extra oxide (xO), which is below the detection limits of the TGA and diffraction techniques. This excess oxygen cannot be accommodated in the c′-BaO_2 layer because the O4 "tetrahedral" oxide site completely blocks any simultaneous occupancy of the O5 "octahedral" oxide site, and thus for this extra oxide to be accommodated the entire layer has to transform into the c_p-BaO_{2+x} layer with partial occupancy (slightly above 2/3) of the O5 sites. Under a high p_{O_2} environment (such as in air or O_2), this small amount of excess oxide (xO) is incorporated into the *c*′-BaO_2 layers, thus leading to partial transformation from the c′-BaO_2 layers to the c_p-BaO_{2+x} layers as described by reaction 1, producing a mixture of c′-BaO_2 and c_p-BaO_{2+x} layers for the as-synthesized and reoxidized samples. Once the sample is under a low p_{O_2} environment (such as dynamic or static vacuum), reaction 1 shifts to the left, forming c′-BaO_2 layers. For the as-synthesized sample 2 sealed in the silica tube, oxygen loss occurs at high temperature as a result of equilibration with the gas phase, and the c_p-BaO_{2+x} layers transform into c′-BaO_2 layers. During the cooling process, this oxygen released by the limited reduction at high temperature in the isolated environment is reabsorbed into the c′-BaO_2 layers to reform mixed c′-BaO_2 and c_p-BaO_{2+x} layers. The fact that the oxygen vacancy ordered c′-BaO_2 layers can transform into oxygen vacancy disordered c_p-BaO_{2+x} layers due to slight excess of oxygen in $Ba_7Y_2Mn_3Ti_2O_{20}$ could account for the limited ionic conduction behavior for this material, which will be discussed in the final section.

O4 Site Splitting. Refinements of both vacancy ordered and disordered phases indicate that the O4 atoms associated with the tetrahedral M2 site in all the structures are disordered over the general 36i position around the 3-fold axis rather than occupying the ideal 6c sites: the distance between the 36i and 6c sites is 0.38−0.43 Å. The site splitting of the O4 atoms must be highly correlated with the repulsion from Ba4 and M2 cations, which are on the 3-fold axis (in Figure 10). Occupation of the 6c sites by oxygen would lead to short Ba4−O4 and M2−O4 bond lengths, for example, 2.41(1) Å for Ba4−O4 and 1.65(1) Å for M2−O4 in the

Table 5. BVSs for Y^{3+}, Ti^{4+}, and Mn^{4+} in the Structure of $Ba_7Y_2Mn_3Ti_2O_{20}$ Sample 1 at Ambient Temperature

	as-synthesized ($Y3^+$ BVS of 3.62)		reduced ($Y3^+$ BVS of 3.60)	
	Ti^{4+} (deviation)	Mn^{4+} (deviation)	Ti^{4+} (deviation)	Mn^{4+} (deviation)
M1	4.61 (15.25%)	3.90 (2.5%)	4.50 (12.5%)	3.81 (4.75%)
tetrahedral M2′	4.39 (9.75%)	3.71 (7.25%)	4.28 (7%)	3.62 (9.5%)
pyramidal M2″	3.92 (2%)	3.31 (17.25%)		
M3	4.43 (10.75%)	3.75 (6.25%)	4.29 (7.25%)	3.63 (9.25%)

as-synthesized sample 1. The O4 anion is thus disordered to produce acceptable values of these distances.

B Site Ordering. It is difficult to determine the occupancies of the Ti and Mn cations at the M1, M2, and M3 sites from XRD and NPD data because of their similar scattering lengths, but the distribution can be analyzed in light of the normal coordination environments and BVSs of Ti and Mn cations. The Mn cation has an oxidation state of +4 in $Ba_7Y_2Mn_3Ti_2O_{20}$, which is confirmed by the TGA data and the effective moment per Mn. The BVSs of Ti^{4+} and Mn^{4+} on M1, M2, and M3 sites for the ambient temperature structure of as-synthesized and reduced $Ba_7Y_2Mn_3Ti_2O_{20}$, listed in Table 5, are consistent with Mn having a greater occupancy than Ti at the central M1 site in the trimer of face-sharing octahedra (FSO). Mn atoms prefer the M3 sites (the outer site in the trimer), and Ti atoms prefer the M2 sites (the tetrahedral and pyramidal sites). For Mn, tetrahedral coordination is only observed for Mn^{5+}, Mn^{6+}, and Mn^{7+}, but face-sharing octahedral coordination is quite common for Mn^{4+}. Furthermore, the good agreement of the observed with the spin-only magnetic moment for Mn^{4+} suggests that mixed MnO_4 and Mn_3O_{12} units are not present. Tetrahedral Ti^{4+} cations are not common but are observed in Ba_2TiO_4[29,30] and $Ba_6R_2Ti_4O_{17}$ (R = Nd and Y).[14] Face-sharing Ti^{4+} species are only observed in the form of dimers because of the strong electrostatic repulsion that would occur in higher-order assemblies. Therefore, it is reasonable to propose a site ordering along the *c*-axis for $Ba_7Y_2Mn_3Ti_2O_{20}$ as isolated TiO_4 tetrahedra or corner-sharing TiO_5 pyramids connected by corner-sharing with YO_6 octahedra, which in turn share corners with face-sharing Mn_3O_{12} trimers. The emergence of the 12R-phase ($Ba_4YMn_3O_{11.5}$)[22] as a second phase with increasing substitution of Ti by Mn in $Ba_7Y_2Mn_{3+x}Ti_{2-x}O_{20}$ ($x = 1, 2$) and the disappearance of the 21R-phase at the nominal composition $Ba_7Y_2Mn_5O_{20}$ confirms the strong preference of the Ti^{4+} cations in $Ba_7Y_2Mn_3Ti_2O_{20}$ for the M2 sites, which could stabilize this 21R-type structure. The BVS (Table 5) suggests over-bonding for the Ti^{4+} at tetrahedral M2′ sites (~4.39) in the as-synthesized sample compared with that (~4.28) in the reduced sample. This could be due to the disordered c′-BaO_2 and c_p-BaO_{2+x} layers in the as-synthesized sample, because the presence of the c_p-BaO_{2+x} layers makes the average distance of c′-BaO_2 layers from neighboring c-BaO_3 layers shorter in the average structure than will be the case locally.

The short M1−M3 distances 2.507(5) Å and 2.530(6) Å in the as-synthesized and reduced samples respectively agree well with those observed in $Ba_4YMn_3O_{11.5}$ (2.502(2)Å) within the FSO trimer.[22] These distances are slightly shorter than those in the trimer of FSO of the 12R-hexagonal phase of $BaMn_{1/2}Ti_{1/2}O_3$ (2.552(1) Å),[24] where the outer trimer sites are shared by 50% Mn and 50% Ti and the central trimer site is 100% Mn reflecting the previously noted absence of Ti trimers in such units. The distances are much shorter than the Ti−Ti distances in the FSO dimer for 6H-$BaTiO_3$ and 12H-$Ba_6R_2Ti_4O_{17}$ (2.69(1)Å for R = Nd and 2.722(6)Å for R = Y).[14] The tetrahedral bond lengths for $Ba_7Y_2Mn_3Ti_2O_{20}$ of 1.70−1.83 Å are consistent with those observed in Ba_2TiO_4 (1.79−1.83 Å) and $Ba_6R_2Ti_4O_{17}$ (1.70−1.82 Å) rather than with those in $Mn^{5+/6+/7+}O_4$ (1.57−1.79 Å).[23,28,31] All the bond length information above is consistent with the proposed site occupation: Ti and Mn are essentially ordered and distributed on tetrahedral and pyramidal M2 sites and FSO trimer sites respectively to form TiO_4 or TiO_5 and Mn_3O_{12} units. As the transformation between c′-BaO_2 and c_p-BaO_{2+x} layers in $Ba_7Y_2Mn_3Ti_2O_{20}$ requires the introduction of a small amount of extra oxygen and associated oxidation to Mn^{5+}, the possibility of a small amount of Ti/Mn disordering involved in the tetrahedral site cannot be entirely excluded. There is a precedent for octahedral Mn^{5+} in $Ba_4Mn_2NaO_9$,[32] which means that tetrahedral Mn is not required for oxidation to take place.

Mixed Conduction. As seen in the 12H-type $Ba_6Y_2Ti_4O_{17}$, 21R $Ba_7Y_2Mn_3Ti_2O_{20}$ also exhibits mixed electronic−ionic conduction at high temperature. The bulk conductivity σ_b at 700 °C in air reaches ~ 2.6×10^{-3} Ω^{-1} cm^{-1}, which is comparable with that of $Ba_6Y_2Ti_4O_{17}$.[15] The oxygen ion transport number for $Ba_7Y_2Mn_3Ti_2O_{20}$ of 0.37−0.40 in 873−1073 K, estimated from the O_2/air concentration cell, is comparable with that of $Ba_6Y_2Ti_4O_{17}$ (0.35) but is smaller than that of the cubic perovskites, for example, Fe-doped $La_{1-x}Sr_xGaO_3$ (0.6 for $La_{0.7}Sr_{0.3}Ga_{0.6}Fe_{0.4}O_3$).[33] The p-type conduction arises from holes (either localized at Mn^{4+} or on minor impurity atoms, for example, Fe^{3+} on Ti^{4+} and Mn^{4+} sites) and is consistent with the incorporation of excess oxygen at high oxygen partial pressures. The calculated slope of the log $\sigma_b \sim \log(p_{O_2})$ plot over the p_{O_2} range of $1-10^{-4}$ atm is 0.13, which is smaller than that (0.25) for a simple equilibrium with monoionized defects.

The refinement of the high-temperature NPD data indicates that there are no significant oxygen vacancies in the h-BaO_3 layer and around the YO_6 octahedron (O1, O2, and O3 atoms), consistent with the strong preference of Y^{3+} for octahedral coordination. Therefore the oxygen ionic conduction observed for this material should be due to motion of oxide in the c′-BaO_2 layers, although the vacancies are

(29) Wu, K. K.; Brown, I. D. *Acta Crystallogr., Sect. B* **1973**, *29*, 2009.
(30) Gunter, J. R.; Jameson, G. B. *Acta Crystallogr., Sect. C* **1984**, *40*, 207.
(31) Floros, N.; Hervieu, M.; Michel, C.; Perez, O.; Raveau, B.; Suard, E. *Solid State Sci.* **2002**, *4*, 627.
(32) Quarez, E.; Roussel, P.; Pérez, O.; Leligny, H.; Bendraoua, A.; Mentré, O. *Solid State Sci.* **2004**, *6*, 931.
(33) Ishihara, T.; Tsuruta, Y.; Yu, C.; Todaka, T.; Nishiguchi, H.; Takita, Y. *J. Electrochem. Soc.* **2003**, *150* (1), E17.

ordered in the c′-BaO_2 layer on average in the material with the exact O_{20} composition. As revealed by the structure refinement of the NPD data, the oxygen vacancy ordered c′-BaO_2 layers in $Ba_7Y_2Mn_3Ti_2O_{20}$ can be partially transformed to the c_p-BaO_{2+x} layers with ∼1/3 disordered oxygen vacancies. These disordered oxygen vacancy c_p-BaO_{2+x} layers could provide a mechanism for the oxygen mobility. This may also be applied to 12H-$Ba_6R_2Ti_4O_{17}$. At high temperature, the oxygen atoms can hop within the c_p-BaO_{2+x} layers. This material, as well as $Ba_6Y_2Ti_4O_{17}$, has a relatively low oxygen ion transport number compared with that for cubic perovskites with three-dimensional oxygen vacancies, which could be due to the constraint of the oxygen mobility pathway to occur solely within the two-dimensional c_p-BaO_{2+x} layers. The oxygen mobility might be also be reduced by strong covalent bonding with the B-cations neighboring the c_p-BaO_{2+x} or c′-BaO_2 layers, and therefore the substitution of the B-cations with less covalent elements would be an appropriate way to try to improve the ionic conduction contribution for future work.

The low conductivity and oxygen ion transport number and instability under low p_{O_2} environment at high temperature precludes this material from applications in SOFCs. This study does however demonstrate the potential of oxygen deficient hexagonal perovskites with ordered oxygen vacancies in cubic layers to provide ionic conduction. Future work should focus on improved redox stability by introducing structural units that are favored by Mn^{3+} or Mn^{2+}: the FSO trimer here is unique to Mn^{4+} and would have to decompose to permit significant reduction in response to lowering p_{O_2}.

Conclusion

The structural characterization of the 21R-type mixed conducting hexagonal oxygen-deficient perovskite $Ba_7Y_2Mn_3Ti_2O_{20}$ by variable temperature NPD has identified intergrowth of oxygen vacancy ordered c′-BaO_2 layers and oxygen vacancy disordered c_p-BaO_{2+x} layers in the oxygen-deficient layers and transformation between the c′-BaO_2 layers and c_p-BaO_{2+x} layers by a redox mechanism. For the as-synthesized sample, there are mixed c′-BaO_2 layers with TiO_4 units (∼62%) and c_p-BaO_{2+x} layers with TiO_5 units (∼38%) sharing corners between adjacent layers which are distributed in a disordered manner in the oxygen deficient layers, and the stacking sequence of c-BaO_3, h-BaO_3, and c′-BaO_2 layers or c_p-BaO_{2+x} layers is $(cc(c'/c_p)cch_2)_3$ along the *c*-axis. Once under a slightly reducing environment, the c_p-BaO_{2+x} layers transform into c′-BaO_2 layers, and the stacking sequence of c-BaO_3, h-BaO_3 and c′-BaO_2 layers becomes $(ccc'cch_2)_3$. The structure of $Ba_7Y_2Mn_3Ti_2O_{20}$ is consistent with Mn^{4+} cations preferring face-sharing octahedral sites to form Mn_3O_{12} trimers, Ti^{4+} cations occupying sites between c′ or c_p and c layers to form TiO_4 tetrahedra or TiO_5 pyramids, and Y^{3+} cations occupying octahedral sites between c layers. The oxygen atoms in the c′-BaO_2 layers show site splitting around the 3-fold axis, which is due to short contacts to the Ba4 and M2 cations on the 3-fold axis. The existence of the c′-BaO_2 layers could be responsible for the observed ionic conduction at high temperature for this material, as the c′-BaO_2 layers with ordered oxygen vacancies can transform to c_p-BaO_{2+x} layers with disordered oxygen vacancies. This provides the potential for oxygen mobility and an oxygen hopping path. This mechanism should stimulate the search for new materials with c′-BaO_2 layers exhibiting better mixed conductor or even pure ionic conductor behavior.

Acknowledgment. The authors thank Dr. Craig Bridges for his help with magnetic property measurement and Dr. Zhengxin Wang and Ann Leyden for their help with collecting the infrared data. The authors thank EPSRC for funding under EP/C511794.

Supporting Information Available: Schematic plot of the concentration cell for oxygen transport number measurement; hydrogen-reduction TGA data; Rietveld plot for XRD data of as-synthesized $Ba_7Y_2Mn_3Ti_2O_{20}$; difference Fourier maps in color replotted by MAPVIEW in WINGX package for the as-synthesized and the reduced $Ba_7Y_2Mn_3Ti_2O_{20}$ sample 1; Ba−O bond lengths (Å) for the as-synthesized and reduced $Ba_7Y_2Mn_3Ti_2O_{20}$ sample 1 at ambient temperature; final structural parameters and selected atomic distances and bond angles for $Ba_7Y_2Mn_3Ti_2O_{20}$ unsealed at 873 K; the experimental and calculated complex impedance $Z''-Z'$ plot and $Y''-f$ and $C''-f$ bode plots for a $Ba_7Y_2Mn_3Ti_2O_{20}$ pellet at 398 K; the p_{O_2} dependence of bulk conductivity for $Ba_7Y_2Mn_3Ti_2O_{20}$ ceramic at 873 K; and infrared absorption data for $Ba_7Y_2Mn_3Ti_2O_{20}$ with $Ba_7Ca_2Mn_5O_{20}$ as comparison (PDF). This material is available free of charge via the Internet at http://pubs.acs.org.

CM0626740